Thermalization of velocity-selected excited-state populations by resonance exchange collisions and radiation trapping

J. Huennekens, R. K. Namiotka, J. Sagle, and Z. J. Jabbour*
Department of Physics, Lehigh University, 16 Memorial Drive East, Bethlehem, Pennsylvania 18015

M. Allegrini†
Dipartimento di Fisica, Università di Pisa, Piazza Torricelli 2, 56126 Pisa, Italy
(Received 27 December 1994)

Populations of excited atoms that all have the same z component of velocity can be produced by pumping a vapor with a narrow-band laser. This velocity-selected population is then thermalized by velocity-changing collisions. However, in a pure vapor, even at low densities where velocity-changing collisions can be ignored, the mechanisms of radiation trapping and resonance exchange collisions can still lead to substantial thermalization of excited-atom velocity distributions. In this paper, we present data demonstrating these effects. We compare our data with results from a simple model of these processes. The model is in qualitative agreement with the experimental results.

PACS number(s): 32.70.Jz, 34.90.+q

INTRODUCTION

Single-mode tunable lasers have linewidths that are typically much smaller than the thermal Doppler width of spectral lines of atoms in a vapor. Collisional and natural linewidths in a vapor are also typically narrower than the Doppler width. Under these conditions, a narrow velocity group can be pumped, creating a population of excited-state atoms that all have the same component of velocity along the pump-laser propagation direction. Velocity-selective pumping has important applications in saturation spectroscopy [1–3], line shape studies [4,5], laser cooling of atoms [6–8], and the study of velocity-changing collisions [9,10].

It is common to assume that the principal destruction mechanism of the narrow excited-state velocity distribution created by the laser pumping is velocity-changing collisions (VCC). For the specific case of velocity-selective excitation of the cesium $6P_J$ levels, which is of interest in the present work, velocity-changing collisions can be represented by the following:

$$\mathrm{Cs}(6P_J, v_z) + M \rightarrow \mathrm{Cs}(6P_J, v_z') + M \ . \tag{1}$$

Here M is the collision partner, v_z is the component of velocity along the laser propagation (z) direction initially selected by the narrow-band laser pumping, and v_z' is the final (random) velocity component after the collision. Velocity-changing collisions do indeed constitute the principal mechanism for thermalization of the excited-state velocity distribution when the ground-state density of the atoms of interest (i.e., cesium) is low, but when there is a relatively large density of foreign or buffer gas atoms. However, when the vapor consists only of atoms of the one species of interest, and when the velocity-selective pumping is carried out using a strong, dipole-allowed transition coupling to the ground state, then the two additional mechanisms of resonance exchange (RE) and radiation trapping can play an important role in the thermalization of the excited-state population. These processes are important because they mimic the effects of velocity-changing collisions, but occur at low densities of the atoms that absorb and emit photons and low foreign-gas atom densities where velocity-changing collisions are expected to be insignificant. In this paper, we discuss these two mechanisms and present data that demonstrate some of their effects.

THEORY

Resonance exchange is a collisional process involving one ground-state and one excited-state atom of the same species [11,12]. In the collision, the excitation is transferred from the initially excited atom to the other atom:

$$\mathrm{Cs}(6P_J, \vec{v}) + \mathrm{Cs}(6S_{1/2}, \vec{v}') \rightarrow \mathrm{Cs}(6S_{1/2}, \vec{v}) + \mathrm{Cs}(6P_J, \vec{v}') \ . \tag{2}$$

Thus the velocity-selected excited atom is replaced by a non-velocity-selected atom as a result of the excitation transfer process. Note that this process does not require a deflection of the atom trajectories, and thus it is different from velocity-changing collisions. Instead, process (2) appears to be similar to excitation transfer collisions involving two atoms of different species; i.e., $A^* + B \rightarrow A + B^*$. However, process (2) is of a much longer range (i.e., impact parameters on the order of a few hundred Å) because it is mediated by the resonant

*Present address: NIST, Building 220, Room B206, Gaithersburg, MD 20899.

†Present address: Dipartimento di Fisica della Materia, Geofisica e Fisica dell'Ambiente, Università di Messina, Salita Sperone 31, 98166 Sant'Agata (Messina), Italy.

exchange of photons between two atoms with degenerate energy levels [13–15].

In the description of resonance exchange, we consider the degenerate two-state basis set constructed from products of atomic states: $\Psi_A(1)\Psi_B(2)$ and $\Psi_B(1)\Psi_A(2)$. Here we label the components of the position and velocity vectors of the first (second) atom collectively by 1 (2), and we denote the electronic states of each atom by the subscripts A and B.

The resonance exchange interaction is due to the long-range dipole-dipole terms in the Hamiltonian, which may be written as

$$V=\frac{1}{R^3}[\vec{D}_1\cdot\vec{D}_2-3(\vec{D}_1\cdot\hat{R})(\vec{D}_2\cdot\hat{R})] . \tag{3}$$

In this expression $\vec{D}_1(\vec{D}_2)$ is the dipole moment operator of atom 1 (atom 2), $\vec{R}$ is the internuclear separation vector, and $\hat{R}$ is a unit vector in the direction of $\vec{R}$. This operator yields nonzero off-diagonal matrix elements with respect to the degenerate-state functions given above if states A and B are connected by a dipole-allowed transition:

$$\langle\Psi_A(1)\Psi_B(2)\left|\frac{1}{R^3}[\vec{D}_1\cdot\vec{D}_2-3(\vec{D}_1\cdot\hat{R})(\vec{D}_2\cdot\hat{R})]\right|\Psi_B(1)\Psi_A(2)\rangle\neq 0 . \tag{4}$$

Thus, degenerate perturbation theory yields a first-order energy splitting of the atomic levels that is equal to twice the absolute magnitude of the matrix element in Eq. (4). Since the splitting scales as R^{-3}, the effects are of a very long range. This resonance exchange is closely related to resonance broadening, which is mediated by the same matrix elements [12]. Carrington, Stacey, and Cooper [12] have calculated resonance exchange rate coefficients for $J=\frac{1}{2}\rightarrow J=\frac{1}{2},\frac{3}{2}$ transitions. In this reference, resonance exchange is referred to as "transfer of population from atom 1 to atom 2."

The other mechanism by which velocity selectivity can be lost is radiation trapping, as depicted in Fig. 1. An atom with a particular velocity component v_z along the laser propagation axis is selectively excited by a narrow-band laser. The atom can fluoresce into any direction, but we will first consider emission in the x direction.

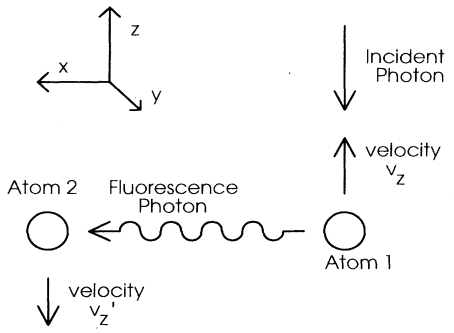

FIG. 1. Thermalization of the excited-atom velocity distribution by radiation trapping. The incident photon from the laser is absorbed by a ground-state atom with well-defined velocity v_z along the laser propagation direction (z axis). The absorbing atom emits a fluorescence photon in a random direction. If the photon is emitted in the x direction (or equivalently in any direction perpendicular to the z axis), the fluorescence photon frequency can be anywhere within the Doppler profile depending on the emitting atom's x component of velocity. This fluorescence photon can be reabsorbed by any atom having the same x component of velocity. However, in general, the second atom's z component of velocity (v_z') is uncorrelated with that of the first atom.

Since the velocity component v_x is not correlated with v_z in a thermalized vapor, the frequency of the emitted photon can lie anywhere within the Doppler profile. This photon can be reabsorbed by any atom for which the photon is resonant (i.e., by any atom with the same velocity component v_x). However, the absorbing atom can have any component of velocity (v_z') along the z axis. The net effect of the emission-reabsorption sequence is, therefore, an exchange of the excited-atom velocity class from v_z to v_z'. For emission along directions that are not perpendicular to the z axis, there is some correlation between the absorbed and emitted photon frequencies, and therefore between the initial and final velocity classes v_z and v_z'. However, including the averaging over possible emission directions, it is clear that this process tends to thermalize the excited-atom velocity distribution.

It is interesting to note that resonance exchange and radiation trapping are essentially the same physical process. In both cases, a photon is exchanged between a ground and an excited atom with the net effect of an exchange of velocity class of a member of the excited-state distribution with one from the ground-state distribution. The only difference between the two processes is range: in resonance exchange, one or many virtual photons are exchanged during a long-range collision in the near field where the interaction is not retarded, while in radiation trapping, a real photon is exchanged over possibly macroscopic distances in the far field where retardation effects must be considered [16].

EXPERIMENT

Figure 2 shows a simplified picture of the experimental setup, and a simplified energy-level diagram of cesium is shown in Fig. 3. Cesium vapor is contained in a sealed cylindrical glass cell 70 mm long and 21 mm in diameter, with no buffer gas, which was heated to a temperature in the range 22–100°C. This resulted in cesium densities in the range 3.1×10^{10} to 1.5×10^{13} cm^{-3}, according to the Nesmeyanov vapor pressure formula [17]. A single-mode cw Ti:sapphire laser (Coherent model 899-29, hereafter referred to as the pump laser) was used to excite the atoms from the $6\,^2S_{1/2}$ ground state to either the $6\,^2P_{1/2}$

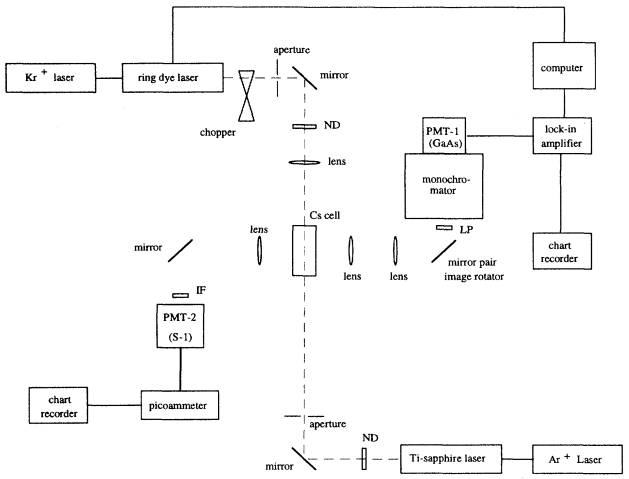

FIG. 2. Experimental setup. IF, LP, ND, and PMT represent interference filter, long pass filter, neutral density filter, and photomultiplier tube, respectively.

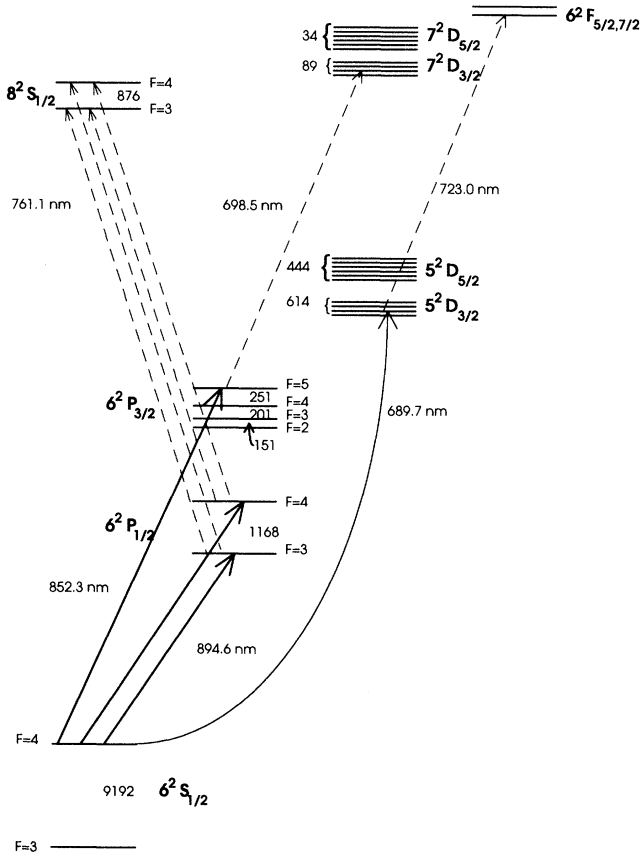

FIG. 3. Schematic energy-level diagram of cesium. Pump transitions are indicated by thick solid lines and probe transitions by dashed lines. The one-photon, quadrupole, pump transition is indicated by a thin solid line. Transition wavelengths are given in nm, and hyperfine splittings in MHz. Hyperfine level splittings have been greatly exaggerated for clarity and are not to scale.

or the $6\,^2P_{3/2}$ excited state (D_1 or D_2 line pumping). The pump beam was roughly collimated and apertured such that its diameter at the cell was ~ 2.0 mm. Typical pump-laser power was 500 and 660 mW for D_1 and D_2 line pumping, respectively, although this was generally reduced by a factor of 2–5 using neutral density filters. The criteria used to set the pump power were that the pump beam had to be sufficiently intense to yield a uniform excitation along the beam path through the cell (i.e., to saturate the transition along the full beam path), but had to be sufficiently weak that it did not cause significant ionization (as evidenced by the observation of recombination radiation from high-lying atomic levels). A counterpropagating single-mode cw dye laser (Coherent model 699-29) was used to probe the excited-atom velocity distribution on the $6\,^2P_{1/2} \rightarrow 8\,^2S_{1/2}$ and $6\,^2P_{3/2} \rightarrow 7\,^2D_{3/2}$ transitions (see Fig. 3). The probe-laser power was typically 140 and 150 mW before the chopper (see Fig. 2) for the $6\,^2P_{1/2} \rightarrow 8\,^2S_{1/2}$ and $6\,^2P_{3/2} \rightarrow 7\,^2D_{3/2}$ transitions, respectively. Neutral density filters were used to attenuate the probe-laser power to a few milliwatts. However, test measurements using probe-laser powers ranging from 150 mW to less than 1 μW showed that the results do not vary systematically with probe intensity. The probe beam was focused with either a 0.5- or a 2-m focal length lens to a Gaussian beam diameter of ~ 0.11 or 1.1 mm, respectively, at the center of the cell. The results were found to be insensitive to the probe beam diameter, and most of the results presented here were obtained with the smaller probe spot size. Over the length of the cell, the probe diameter did not vary significantly.

Absorption of the probe laser was monitored by detecting fluorescence at right angles to the laser propagation direction. Fluorescence from a 0.5-cm strip oriented along the laser propagation direction in the central region of the cell was imaged onto the slits of a 0.22-m monochromator (Spex model 1681). The monochromator used a 1200 groove/mm grating blazed at 500 nm, and the slits were set to 300 μm (1 mm when weaker signals were recorded), yielding a resolution of ~ 1 nm (3 nm). When the $6\,^2P_{1/2} \rightarrow 8\,^2S_{1/2}$ transition was probed, fluorescence was monitored on the $8\,^2S_{1/2} \rightarrow 6\,^2P_{3/2}$ transition. When probing the $6\,^2P_{3/2} \rightarrow 7\,^2D_{3/2}$ transition, we monitored $7\,^2D_{3/2} \rightarrow 6\,^2P_{1/2}$ fluorescence. In either case, total fluorescence transmitted through the monochromator was monitored while scanning the probe laser across the probe transition of interest. The probe beam was chopped and lock-in detection was employed. A free-standing photomultiplier tube, with either a D_1 or D_2 line interference filter placed in front of it, was used to monitor fluorescence resulting from pump-laser excitation to ensure that no frequency drift of that laser had occurred.

RESULTS AND DISCUSSION

Figures 4–6 show typical probe-laser scans recorded on the $6\,^2P_{1/2}(F'=3) \rightarrow 8\,^2S_{1/2}$, $6\,^2P_{1/2}(F'=4) \rightarrow 8\,^2S_{1/2}$, and $6\,^2P_{3/2} \rightarrow 7\,^2D_{3/2}$ transitions as a function of temperature. In each scan, one can recognize narrow features (representing absorption from the velocity class selected

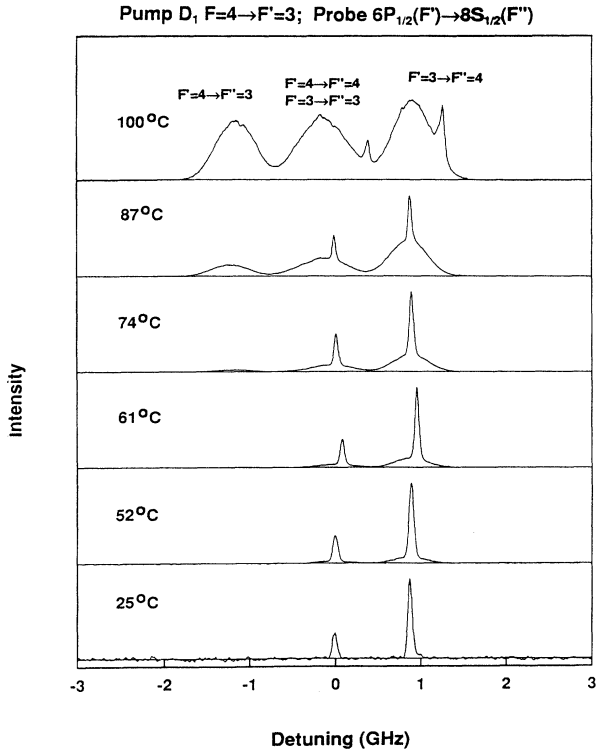

FIG. 4. Excitation spectra probing the velocity distribution in the cesium $6^2P_{1/2}$ state following pumping of the $6^2S_{1/2}(F=4)\rightarrow 6^2P_{1/2}(F'=3)$ resonance transition. The spectra were obtained by monitoring fluorescence on the $8^2S_{1/2}\rightarrow 6^2P_{3/2}$ transition, while scanning the probe laser over the $6^2P_{1/2}\rightarrow 8^2S_{1/2}$ transition. Individual traces correspond to different cell temperatures, which are listed in the figure. In each case, one can see two narrow spikes representing the $6^2P_{1/2}(F'=3)$-state velocity class prepared by the pump laser, and two or three Doppler pedestals created by the thermalizing effects of radiation trapping and resonance exchange (see text). Note that the position of each spike with respect to the corresponding pedestal is shifted at the highest temperature. This position is determined by the detuning of the pump laser, which was set to maximize the total resonance fluorescence signal. At high temperatures, a larger detuning was necessary to avoid absorption of the pump before it reached the observation region. These data were recorded with a probe beam diameter of 0.11 mm.

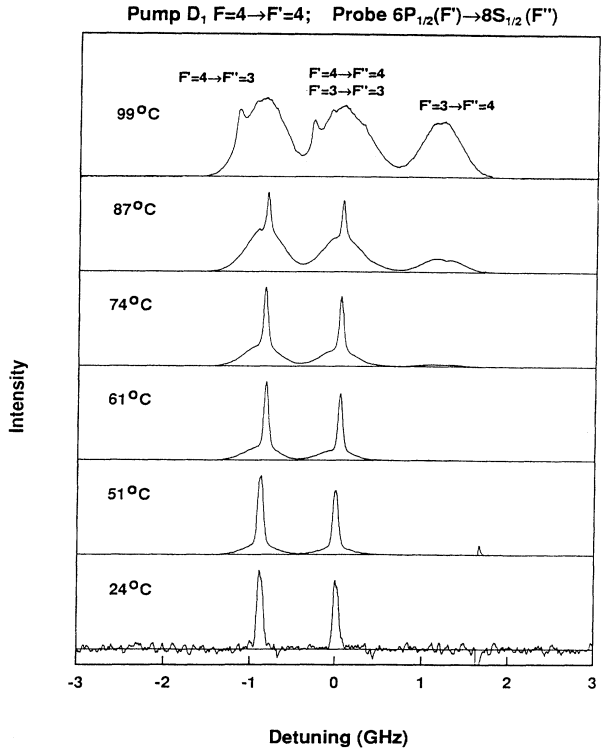

FIG. 5. Excitation spectra probing the velocity distribution in the cesium $6^2P_{1/2}$ state following pumping of the $6^2S_{1/2}(F=4)\rightarrow 6^2P_{1/2}(F'=4)$ resonance transition. The spectra were obtained by monitoring fluorescence on the $8^2S_{1/2}\rightarrow 6^2P_{3/2}$ transition, while scanning the probe laser over the $6^2P_{1/2}\rightarrow 8^2S_{1/2}$ transition. These data were recorded with a probe beam diameter of 0.11 mm.

by the pump laser) superimposed on broad Doppler pedestals. The Doppler-free spikes are broadened somewhat by power broadening, and in the case of the $6^2P_{3/2}\rightarrow 7^2D_{3/2}$ transition, by the unresolved $7^2D_{3/2}$ state hyperfine structure ($\sim$90 MHz total splitting [18]). The $8^2S_{1/2}$ hyperfine splitting of 876 MHz is well resolved in this experiment [18]. [For a counterpropagating two-photon pump-probe sequence using unequal laser frequencies, as in the present experiment, the Doppler shifts of the two transitions do not exactly cancel. As a result, a fraction $1-(\lambda_{7D_{3/2}\rightarrow 6P_{3/2}}/\lambda_{6P_{3/2}\rightarrow 6S_{1/2}})$ of the intermediate $6^2P_{3/2}$ state hyperfine structure also contributes to the broadening of the narrow spike on the $6^2P_{3/2}\rightarrow 7^2D_{3/2}$ transition [19]. In the case of the $6^2P_{1/2}$ state, the hyperfine splitting is sufficiently large that only one of the two hyperfine levels is efficiently pumped. Therefore, this latter broadening mechanism does not contribute in that case.]

As the temperature increases, the Doppler pedestals grow at the expense of the Doppler-free spikes, due to the combined effects of radiation trapping and resonance exchange. Note that from scan to scan the positions of the spikes change relative to the Doppler pedestals. These positions are determined by the exact detuning of the pump laser within the D_1 or D_2 line profiles. The detuning was set to maximize the resonance fluorescence signal. For the D_1 line at low temperatures, the hyperfine structure is well resolved, and the fluorescence maximum occurs when the pump laser is tuned to the line center of the relevant transition. For the D_2 line at low temperatures, the fluorescence maximum occurs when the pump laser is tuned near the peak of the $6^2S_{1/2}(F=4)\rightarrow 6^2P_{3/2}(F'=5)$ transition, since this reduces the optical hyperfine pumping in the ground state. Generally, larger detunings are necessary at higher densities due to increased optical depths. Note also that the complete hyperfine structure of the $6^2P_{1/2}\rightarrow 8^2S_{1/2}$ transition can be observed in Figs. 4 and 5, which differ

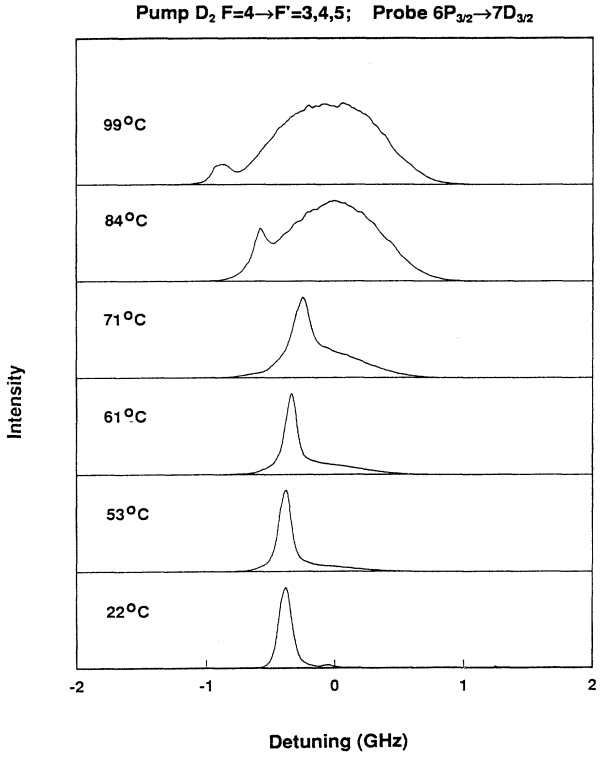

FIG. 6. Excitation spectra probing the velocity distribution in the cesium $6\,^2P_{3/2}$ state following pumping of the $6\,^2S_{1/2}(F=4)\rightarrow 6\,^2P_{3/2}(F'=3,4,5)$ resonance transition. The spectra were obtained by monitoring fluorescence on the $7\,^2D_{3/2}\rightarrow 6\,^2P_{1/2}$ transition, while scanning the probe laser over the $6\,^2P_{3/2}\rightarrow 7\,^2D_{3/2}$ transition. Note that the position of the spike with respect to the pedestal systematically moves from trace to trace. This position depends on the detuning of the pump laser, which was set to maximize the total resonance fluorescence. The position of the maximum is determined by a combination of optical depth and optical pumping effects. These data were recorded with a probe beam diameter of 1.1 mm.

in whether we pumped the $F'=3$ or $F'=4$ hyperfine level of the $6\,^2P_{1/2}$ state, respectively. When pumping the $F'=3$ level, we only observe the $6\,^2P_{1/2}(F'=3)\rightarrow 8\,^2S_{1/2}(F''=3,4)$ transitions at low temperatures and densities. However, at higher densities, $6\,^2P_{1/2}(F'=4)\rightarrow 8\,^2S_{1/2}(F''=3,4)$ transitions can also be observed (the $F'=4\rightarrow F''=4$ transition is not resolved from the $F'=3\rightarrow F''=3$ transition). At these densities, the $6\,^2P_{1/2}(F'=4)$ level is populated by trapping of photons emitted in the wings of the $6\,^2P_{1/2}(F'=3)\rightarrow 6\,^2S_{1/2}(F=3,4)$ transitions.

We can estimate the magnitude of the thermalizing effects of radiation trapping and resonance exchange collisions by measuring the ratio of the intensity in the narrow features and comparing it to that associated with the Doppler pedestals. Experimental values for this ratio are listed in Table I for the three probe transitions studied.

In order to understand these results, we write a rate equation to model the excited-atom population in the velocity class v_z selected by the pump laser,

$$\dot{n}_{6P}(v_z)=0=Pn_{6S}(v_z)-[(k_{\rm VCC}+k_{\rm RE})n_{6S}+\Gamma_{6P\rightarrow 6S}]n_{6P}(v_z)\ , \tag{5}$$

and one to model the total (integrated) population in all other velocity classes v_z',

$$\dot{n}_{6P}(v_z')=0=[(k_{\rm VCC}+k_{\rm RE})n_{6S}+(1-g)f\Gamma_{6P\rightarrow 6S}]n_{6P}(v_z)-g\Gamma_{6P\rightarrow 6S}n_{6P}(v_z')\ . \tag{6}$$

Here P is the rate for velocity-selective excitation due to the pump laser, $k_{\rm VCC}$ and $k_{\rm RE}$ are the rate coefficients for velocity-changing collisions and resonance exchange collisions, respectively, g is the escape factor for $6P\rightarrow 6S$ transition photons (the probability that a fluorescence photon will escape from the region of interest without being absorbed) and $\Gamma_{6P\rightarrow 6S}$ is the natural radiative rate of the $6P\rightarrow 6S$ transition. The factor f is a geometric factor that takes into account the fact that radiation trapping only partially redistributes the z component of velocity if the emission has a component along z. Note that we neglect photon recoil effects and assume a strong collision model (i.e., velocities are randomized by either velocity-changing collisions or resonance exchange collisions). Also, this simple rate equation model neglects transfer of an atom with a thermalized velocity v_z' back into the selected velocity class v_z. However, the "thermalized" component at v_z is properly taken into account by the fitting procedure below.

Equation (6) can be solved for the population (and hence the fluorescence) ratio:

$$\frac{I_{\rm Doppler\ pedestal}}{I_{\rm narrow\ spike}}=\frac{I(v_z')}{I(v_z)}=\frac{n_{6P}(v_z')}{n_{6P}(v_z)}=\frac{(k_{\rm VCC}+k_{\rm RE})n_{6S}+(1-g)f\Gamma_{6P\rightarrow 6S}}{g\Gamma_{6P\rightarrow 6S}}\ . \tag{7}$$

Again, $n_{6P}(v_z')$ is the total population in all velocity classes except v_z, and $I_{\rm Doppler\ pedestal}$ and $I_{\rm narrow\ spike}$ are integrated intensities. Equation (7) is the fundamental equation relating the contributions from velocity-changing collisions, resonance exchange collisions, and radiation trapping to the thermalized and nonthermalized portions of the velocity-dependent line shape.

The escape factor g can be found from radiation trapping theory, although this requires some work in the present geometry. In general, the steady-state excited-atom density $n_{6P}(\vec{r})$ is written as an eigenmode expansion [20–22],

$$n_{6P}(\vec{r})=\sum_j a_j n_j(\vec{r})\ . \tag{8}$$

Each eigenmode is a mathematical solution of the radiation diffusion equation characterized by a single exponential decay rate, $\beta_j=g_j\Gamma_{\rm nat}$. Here, g_j is the escape factor for mode j, and $\Gamma_{\rm nat}$ is the natural radiative rate for the transition of interest. Note that the individual eigenmode

TABLE I. Experimental and calculated values of $I_{\text{Doppler pedestal}}/I_{\text{narrow spike}}$ for the pump and probe transitions listed. The calculated values have been broken into three terms representing velocity-changing collisions, resonance exchange collisions, and radiation trapping. The sum of these three terms is given in the second to last column. The numbers in brackets denote multiplicative powers of ten. Listed experimental values are averages of all values recorded with probe beam diameters of 0.11 and 1.1 mm.

				Calculation				Experiment
T (°C)	n (cm^{-3})	$g_{6P_{1/2}\to 6S_{1/2}}$	f	$\frac{k_{\text{VCC}}n_{6S_{1/2}}}{g_{6P_{1/2}\to 6S_{1/2}}\Gamma_{6P_{1/2}\to 6S_{1/2}}}$	$\frac{k_{\text{RE}}n_{6S_{1/2}}}{g_{6P_{1/2}\to 6S_{1/2}}\Gamma_{6P_{1/2}\to 6S_{1/2}}}$	$\frac{(1-g_{6P_{1/2}\to 6S_{1/2}})f}{g_{6P_{1/2}\to 6S_{1/2}}}$	$\frac{I_{\text{Doppler pedestal}}}{I_{\text{narrow spike}}}$	$\frac{I_{\text{Doppler pedestal}}}{I_{\text{narrow spike}}}$
				Pump D_1 ($F=4\to F'=3$), probe $6P_{1/2}\to 8S_{1/2}$				
24.5	4.01[10]	0.973	0.810	2.28[−7]	6.29[−4]	2.25[−2]	0.0231	~0*
51.5	4.59[11]	0.737	0.814	3.45[−6]	9.50[−3]	2.90[−1]	0.300	~0*
60.5	9.45[11]	0.551	0.817	9.50[−6]	2.62[−2]	6.66[−1]	0.692	0.220
73	2.41[12]	0.299	0.821	4.46[−5]	1.23[−1]	1.93	2.05	1.41
87	6.36[12]	0.123	0.824	2.86[−4]	7.89[−1]	5.88	6.67	6.89
99	1.38[13]	0.054	0.824	1.43[−3]	3.94	14.58	18.52	16.22
				Pump D_1 ($F=4\to F'=4$), probe $6P_{1/2}\to 8S_{1/2}$				
24.5	4.01[10]	0.969	0.810	2.29[−7]	6.31[−4]	2.59[−2]	0.0265	~0*
51.5	4.59[11]	0.720	0.814	3.53[−6]	9.73[−3]	3.17[−1]	0.326	~0*
60.5	9.45[11]	0.519	0.817	1.01[−5]	2.78[−2]	7.57[−1]	0.785	0.553
73	2.41[12]	0.255	0.821	5.23[−5]	1.44[−1]	2.40	2.54	1.64
87	6.36[12]	0.0945	0.824	3.73[−4]	1.03	7.90	8.92	8.91
99	1.38[13]	0.0392	0.824	1.95[−3]	5.37	20.20	25.57	14.23
				Calculation				Experiment
T (°C)	n (cm^{-3})	$g_{6P_{3/2}\to 6S_{1/2}}$	f	$\frac{k_{\text{VCC}}n_{6S_{1/2}}}{g_{6P_{3/2}\to 6S_{1/2}}\Gamma_{6P_{3/2}\to 6S_{1/2}}}$	$\frac{k_{\text{RE}}n_{6S_{1/2}}}{g_{6P_{3/2}\to 6S_{1/2}}\Gamma_{6P_{3/2}\to 6S_{1/2}}}$	$\frac{(1-g_{6P_{3/2}\to 6S_{1/2}})f}{g_{6P_{3/2}\to 6S_{1/2}}}$	$\frac{I_{\text{Doppler pedestal}}}{I_{\text{narrow spike}}}$	$\frac{I_{\text{Doppler pedestal}}}{I_{\text{narrow spike}}}$
				Pump D_2 ($F=4\to F'=3,4,5$), probe $6P_{3/2}\to 7D_{3/2}$				
22	3.12[10]	0.945	0.672	1.62[−7]	6.61[−4]	3.91[−2]	0.0398	~0*
52.5	4.99[11]	0.417	0.683	5.87[−6]	2.40[−2]	9.55[−1]	0.979	0.096
61.5	1.02[12]	0.227	0.686	2.21[−5]	9.00[−2]	2.34	2.43	0.580
70.5	2.01[12]	0.112	0.689	8.81[−5]	3.60[−1]	5.46	5.82	0.935
83.5	5.03[12]	0.0394	0.694	6.27[−4]	2.56	16.92	19.48	14.77
99	1.38[13]	0.0120	0.698	5.64[−3]	23.04	57.47	80.51	36.34

*At low densities, the Doppler pedestals were so small that they could not be distinguished from the wings of the Lorentzians in the fits.

solutions are nonphysical, since (except for the fundamental mode) each has regions of negative amplitude (see, for example, Figs. 1 and 2 of Ref. [21]). Nevertheless, these eigenmodes form a complete set, and any actual excited-atom spatial distribution can be expanded as a linear superposition of them.

In steady state, we can write a rate equation for each mode amplitude:

$$\dot{a}_j = 0 = P_j - g_j \Gamma_{\text{nat}} a_j \ . \tag{9}$$

Here

$$P_j = \frac{A}{V} \int I_{\text{laser}}(\vec{r}) n_j(\vec{r}) d^3\vec{r} = \frac{2\pi L A}{V} \int_0^R I_{\text{laser}}(r) n_j(r) r \, dr$$

is the laser pumping rate for mode j, and in the last step we have considered the specific case of on-axis excitation in a cylindrical cell of radius R, length L, and volume $V=\pi R^2 L$. $I_{\text{laser}}(r)$ is the pump laser transverse spatial profile [measured to be Gaussian in our experiment; i.e., $I_{\text{laser}}(r) \propto \exp(-r^2/r_{\text{pump}}^2)$ with $r_{\text{pump}}=0.099$ cm] and A is a normalization constant. Thus we obtain for the steady-state mode amplitudes

$$a_j = \frac{P_j}{g_j \Gamma_{\text{nat}}} = \frac{2\pi L A}{g_j \Gamma_{\text{nat}} V} \int_0^R I_{\text{laser}}(r) n_j(r) r \, dr \ . \tag{10}$$

We used a focused, coaxial, counterpropagating probe beam that can be described by a Gaussian transverse profile $\exp(-r^2/r_{\text{probe}}^2)$. Since $r_{\text{probe}} \ll r_{\text{pump}}$, R, the number of atoms detected in mode j, is proportional to $a_j n_j(r=0)$. Finally, the effective radiative rate Γ_{eff}, or escape factor g, for the excited atoms in the detection zone is given by a weighted average of the decay rates for the individual eigenmodes,

$$\Gamma_{\text{eff}} = g \Gamma_{\text{nat}} = \frac{\sum_j a_j n_j(0) g_j \Gamma_{\text{nat}}}{\sum_j a_j n_j(0)} = \frac{\sum_j n_j(0) \int_0^R n_j(r) \exp(-r^2/r_{\text{pump}}^2) r \, dr}{\sum_j \frac{n_j(0)}{g_j \Gamma_{\text{nat}}} \int_0^R n_j(r) \exp(-r^2/r_{\text{pump}}^2) r \, dr} \ . \tag{11}$$

In the Appendix, we present calculations of the escape factor based on the relatively simple Milne [23] and Holstein [20,24] theories, which are valid in the limits of low and high optical depths, respectively. These calculations yield low- and high-density approximations for the fluorescence ratio $I_{\text{Doppler pedestal}}/I_{\text{narrow spike}}$, which show the cesium-atom density dependence in these limits.

However, to model the results of the present experiment, which does not fit exclusively into either of the limiting cases discussed above, we use the Molisch *et al.* theory of radiation trapping [22,25]. This theory is based upon numerical integration of the Holstein radiation diffusion equation and yields analytic fitting equations for the escape factors and eigenmodes. The Molisch results are only slightly more difficult to use than those of Milne and Holstein, and reduce to these latter results in the appropriate limits. Most important, Molisch *et al.* give escape factors for the ten lowest eigenmodes, which allow an accurate expansion of the pump-laser spatial profile in Eqs. (10) and (11).

According to Molisch *et al.* [25], the eigenfunctions for a cylindrical geometry are given by

$$n_j(r) = \frac{1}{R} \left[\frac{2}{J_0^2(\lambda_j) + J_1^2(\lambda_j)} \right]^{1/2} J_0 \left[\lambda_j \frac{r}{R} \right] , \tag{12}$$

where $J_0(x)$ and $J_1(x)$ are the zero- and first-order Bessel functions of the first kind [26], and λ_0 is given by

$$\lambda_0 = d_1 \left[\frac{k_0 R + d_2}{k_0 R + d_2 d_3} \right]^{d_4} . \tag{13}$$

Other values of λ_j are determined from the orthogonality relation

$$\lambda_j \frac{J_1(\lambda_j)}{J_0(\lambda_j)} = \lambda_0 \frac{J_1(\lambda_0)}{J_0(\lambda_0)} \tag{14}$$

and the constants d_1, d_2, d_3, and d_4 are tabulated in Table 3 of Ref. [25].

Finally, for the case where the radiation trapping is dominated by the Doppler core of the line (as in the present case), the escape factor for the jth mode is given according to Molisch *et al.* [25] by the expression

$$g_j^D = \left[1 + \frac{1}{m_j^D} k_0 R \left[\ln \left[\frac{k_0 R}{2} + e \right] \right]^{1/2} - \frac{c_{0j}^D k_0 R \ln(k_0 R) + c_{1j}^D k_0 R + c_{2j}^D (k_0 R)^2}{1 + c_{3j}^D k_0 R + c_{4j}^D (k_0 R)^2} \right]^{-1} . \tag{15}$$

Again, the coefficients m_j^D and c_{ij}^D for the first ten modes are tabulated in Table 1 of Ref. [25]. (The superscript D stands for Doppler line shape.) Note that the escape factor g_j^D used here is the inverse of the Molisch trapping factor g defined in Ref. [25].

We used Eqs. (12)–(14) to calculate the Molisch Doppler line-shape cylinder eigenfunctions, and numerically expanded the pump-laser Gaussian spatial profile in terms of them. We then used this information, along with the lowest ten mode escape factors from Eq. (15) in Eq. (11) to calculate the radiative escape factor of each hyperfine transition. The average escape factor g, appearing in Eq. (7), for the population of excited atoms detected using the probe laser, was obtained from the relation

$$g = \frac{\Gamma_{\text{eff}}}{\Gamma_{6P_J \to 6S_{1/2}}} = \frac{g_{6P_J(F') \to 6S_{1/2}(F=3)} \Gamma_{6P_J(F') \to 6S_{1/2}(F=3)} + g_{6P_J(F') \to 6S_{1/2}(F=4)} \Gamma_{6P_J(F') \to 6S_{1/2}(F=4)}}{\Gamma_{6P_J \to 6S_{1/2}}} , \tag{16}$$

where the upper state is the $F'=3$ or 4 hyperfine level for D_1 line pumping, and is a combination of the $F'=3$, 4, and 5 hyperfine levels for D_2 line pumping. This approach for incorporating hyperfine structure into the trapping calculations is valid because the ground-state hyperfine levels are well separated.

The factor f in Eq. (7) takes into account the fact that radiation trapping only partially redistributes the z component of velocity if the emission direction has a component along z. To calculate f, we first note that the probability of emission in the (θ,ϕ) direction (where θ is the polar angle and ϕ is the azimuthal angle, with respect to the z axis) is $\sin\theta\, d\theta\, d\phi/4\pi$. Next, we note that if an atom emits a photon in direction (θ,ϕ) that is absorbed by another atom, then both emitting and absorbing atoms must have the same velocity component along (θ,ϕ). Setting $v'(\theta,\phi)=v(\theta,\phi)$ (where unprimed and primed velocity components refer to the absorbing and emitting atom, respectively) yields

$$v_x\sin\theta\cos\phi+v_y\sin\theta\sin\phi+v_z\cos\theta = v_x'\sin\theta\cos\phi+v_y'\sin\theta\sin\phi+v_z'\cos\theta\ , \tag{17}$$

and this can be solved for $|v_z-v_z'|$:

$$|v_z-v_z'|=|(v_x'-v_x)\tan\theta\cos\phi +(v_y'-v_y)\tan\theta\sin\phi|\ . \tag{18}$$

We calculated $|v_z-v_z'|$ by selecting an emission direction (θ,ϕ), and velocity components v_x, v_x', v_y, and v_y' from the Gaussian velocity distribution. We counted the emission-reabsorption event as "thermalizing" if the resulting redistribution of the z component of velocity is sufficient to produce a Doppler shift that is greater than the homogeneous linewidth $\Delta\nu$; i.e., if $|v_z-v_z'|>\lambda\Delta\nu$. Here the homogeneous linewidth $\Delta\nu$ is due to natural, self, and power broadening, and in the case of D_2 line pumping, also to unresolved hyperfine structure. Experimentally, we found $\Delta\nu\sim 60$ MHz for D_1 and ~ 110 MHz for D_2 line pumping. Finally, we averaged over emission coordinates and velocity components, with appropriate weighting, to obtain the factor f representing the probability that the emission-reabsorption event is thermalizing. For the D_1 line, the emission is isotropic and the calculation simplified, since we could set $\phi=0$ in Eq. (18). For the D_2 line, the emission is not isotropic. If we assume that the laser is linearly polarized along the y axis, then it can be shown that an additional weighting factor, $\frac{5}{4}-\frac{3}{4}\sin^2\theta\sin^2\phi$, is required, and the full angular average over both θ and ϕ is necessary. We note that, in the calculation of the factor f, we have ignored hyperfine structure and considered the angular emission patterns for pure $J=\frac{1}{2}\rightarrow J=\frac{1}{2}$ and $J=\frac{3}{2}\rightarrow J=\frac{1}{2}$ transitions. In the case of D_2 line pumping this is a necessary approximation, since the upper-state hyperfine level populations are not known. However, the uncertainty introduced into the model due to this approximation is clearly small compared to that from other sources (as discussed below).

The calculation of the factor f depends weakly on the temperature (which determines the width of the Gaussian velocity distributions), and more strongly on the homo-

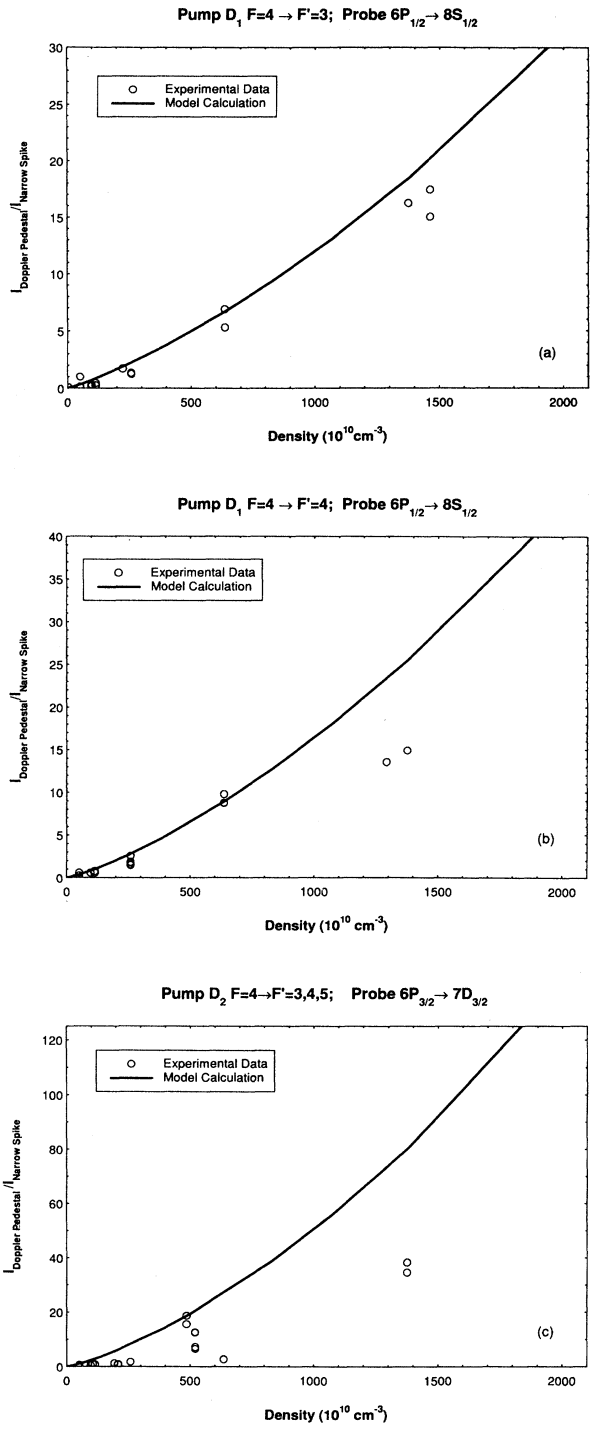

FIG. 7. Plots of $I_{\text{Doppler pedestal}}/I_{\text{narrow spike}}$ versus cesium density. (a) Pump laser tuned to the $6\,^2S_{1/2}(F=4)\rightarrow 6\,^2P_{1/2}(F'=3)$ resonance transition; probe laser scanned across the $6\,^2P_{1/2}\rightarrow 8\,^2S_{1/2}$ transition. (b) Pump laser tuned to the $6\,^2S_{1/2}(F=4)\rightarrow 6\,^2P_{1/2}(F'=4)$ resonance transition; probe laser scanned across the $6\,^2P_{1/2}\rightarrow 8\,^2S_{1/2}$ transition. (c) Pump laser tuned to the $6\,^2S_{1/2}(F=4)\rightarrow 6\,^2P_{3/2}(F'=3,4,5)$ resonance transition; probe laser scanned across the $6\,^2P_{3/2}\rightarrow 7\,^2D_{3/2}$ transition. The solid lines represent values of the ratio $I_{\text{Doppler pedestal}}/I_{\text{narrow spike}}$ calculated using the model described in the text.

geneous (Lorentzian) linewidth. Values of f, calculated in the manner described for the conditions of our experiment, can be found in Table I.

Figures 7(a)–7(c) show the dependence of the measured fluorescence ratios on atom density along with the theoretical ratios obtained from Eq. (7). Some of these experimental and theoretical data are also listed in Table I. For each scan, the data were fit by a sum of Gaussians (for the thermalized Doppler pedestals) and Lorentzians (for the narrow spikes). Doppler widths are in good agreement with those calculated from the temperature for the $6\,^2P_{1/2} \rightarrow 8\,^2S_{1/2}$ line, and are also in good agreement for the $6\,^2P_{3/2} \rightarrow 7\,^2D_{3/2}$ transition when the hyperfine structure of both levels is taken into account. In the calculations, we used the following values: $k_{VCC} = 1.6 \times 10^{-10}$ cm^3 s^{-1} (corresponding to a typical velocity-changing collision cross section of 50 Å^2) [9], and $k_{RE} = 4.41 \times 10^{-7}$ and 6.53×10^{-7} cm^3 s^{-1} for $6\,^2P_{1/2}$ and $6\,^2P_{3/2}$, respectively (from Ref. [12]). In the table, the calculated values are divided into three terms representing velocity-changing collisions, resonance exchange collisions, and radiation trapping. Under our conditions, the fluorescence ratio is always dominated by the radiation trapping term, although the resonance exchange term makes a noticeable contribution. For a pure metal vapor, it can be seen that resonance exchange and radiation trapping are several orders of magnitude more effective than velocity-changing collisions at thermalizing the velocity-selected excited atom distribution.

In analyzing our results, we must also consider the effects of velocity-changing collisions due to impurities in the cell. From other work with this cell [27], we have estimated the impurity density to be less than 10^{14} cm^{-3}. Using a velocity-changing collision rate coefficient $k_{VCC} = 1.6 \times 10^{-10}$ cm^3 s^{-1}, we find that such collisions contribute at a rate that might be comparable to the resonance exchange term at room temperature, but which is totally negligible at higher temperatures. In addition, a constant impurity contribution should produce a pedestal-to-spike intensity ratio that is independent of temperature.

We carried out two additional experiments to verify our interpretation. First, we pumped the impurity cesium $6\,^2S_{1/2} \rightarrow 6\,^2P_{1/2}$ and $6\,^2S_{1/2} \rightarrow 6\,^2P_{3/2}$ transitions in a nominally pure rubidium cell. We then probed the $6\,^2P_{1/2}$ and $6\,^2P_{3/2}$ state velocity distributions as before. An example of the resulting spectra at $T = 139$°C is shown in Fig. 8. At this temperature, the rubidium density is 5×10^{13} cm^{-3}, and therefore the collision rate is comparable to that of pure cesium at $T = 120$°C. However, in this case the excited cesium atoms collide with ground-state rubidium and the two collision partners have energy levels that are not degenerate. Therefore the resonance exchange mechanism is not operative. In addition, radiation trapping does not cause much thermalization because there are few ground-state cesium atoms available to absorb the resonant photons. Figure 8 shows that, under these conditions, the thermalization of the cesium excited-state velocity distribution is dramatically reduced compared to the pure Cs case. The small amount of thermalization evident in Fig. 8 results from

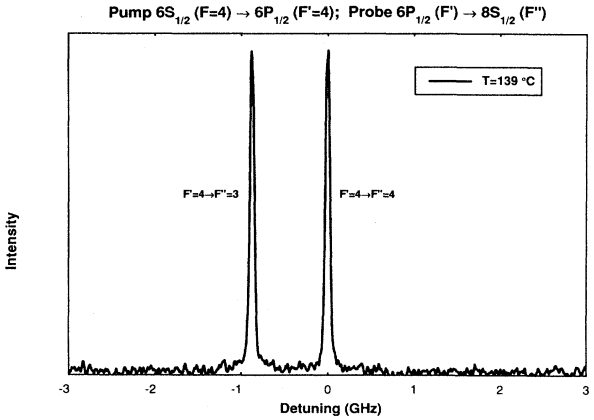

FIG. 8. Excitation spectrum probing the velocity distribution in the cesium $6\,^2P_{1/2}$ state following pumping of the cesium $6\,^2S_{1/2}(F=4) \rightarrow 6\,^2P_{1/2}(F'=4)$ resonance transition in a cell which nominally contains pure rubidium with only a trace of cesium impurity. The spectrum was obtained by monitoring fluorescence on the cesium $8\,^2S_{1/2} \rightarrow 6\,^2P_{3/2}$ transition, while scanning the probe laser over the $6\,^2P_{1/2} \rightarrow 8\,^2S_{1/2}$ transition. The cell temperature was 139°C. Other experimental parameters were similar to those used to obtain the data of Fig. 5.

radiation trapping and resonance exchange collisions involving the cesium impurity atoms, and velocity-changing collisions with ground-state rubidium.

The second test involved the direct pumping of the cesium $5\,^2D_{3/2}$ level on the one-photon, dipole-forbidden but electric-quadrupole-allowed $6\,^2S_{1/2} \rightarrow 5\,^2D_{3/2}$ transition at 689.7 nm in the pure cesium cell. The $5\,^2D_{3/2}$ level velocity distribution was then probed on the $5\,^2D_{3/2} \rightarrow 6\,^2F_{5/2}$ transition at 723.1 nm. Fluorescence was monitored on the $6\,^2F_{5/2,7/2} \rightarrow 5\,^2D_{5/2}$ transition at

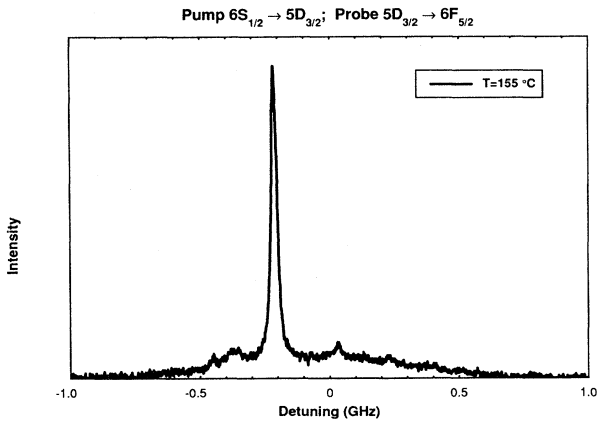

FIG. 9. Excitation spectrum probing the velocity distribution in the cesium $5\,^2D_{3/2}$ state following pumping of the dipole-forbidden, but electric-quadrupole-allowed $6\,^2S_{1/2}(F=4) \rightarrow 5\,^2D_{3/2}(F'=2,3,4,5)$ transition in cesium vapor at $T = 155$°C. The spectrum was obtained by monitoring fluorescence on the $6\,^2F_{5/2,7/2} \rightarrow 5\,^2D_{5/2}$ transition at 728.2 nm, while scanning the probe laser over the $5\,^2D_{3/2} \rightarrow 6\,^2F_{5/2}$ transition at 723.1 nm. The pump- and probe-laser powers were 65 and 110 mW, respectively. Because the signals were weak due to pumping the quadrupole transition, the monochromator slits were opened to 6 mm in this case.

728.2 nm. The spectrum recorded at $T=155$°C is shown in Fig. 9. Again it can be seen that very little thermalization takes place under these conditions, even though $n_{Cs}=2.75\times10^{14}$ cm^{-3} is approximately 20 times greater than in the highest temperature traces of Figs. 4–6. Here the resonance exchange mechanism is inoperative because the colliding $6\,^2S_{1/2}$ and $5\,^2D_{3/2}$ atoms are not in states that are coupled by a dipole-allowed transition. In addition, radiation trapping is negligible in this case because the $5\,^2D_{3/2}$ atoms radiate predominantly to the $6\,^2P_{1/2,3/2}$ levels, which are only weakly populated in this experiment. We note that this experiment also eliminates collisions with impurity atoms as the cause of the thermalization observed in Figs. 4–6, since such collisions would also thermalize the $5\,^2D_{3/2}$-state velocity distribution.

From Table I and Figs. 7(a)–7(c), it is clear that the simple model presented here is in qualitative agreement with our experimental results. In fact, the quantitative agreement is probably better than can be expected, considering that optical hyperfine pumping was not considered in calculating the radiation trapping escape factors. The general situation of radiation trapping in the presence of optical pumping is very difficult to take into account in the model because the optical pumping depends upon the effective radiative rates, which themselves depend on the ground-state hyperfine level populations. However, the latter are not in equilibrium due to the optical pumping. To handle this situation, one must self-consistently solve the optical pumping and radiation trapping equations; most likely through iteration. Even if this is done, the results would be sensitive to the exact laser frequency within the line shape (especially for D_2). Further work is needed to incorporate these effects into the model. As stated earlier, hyperfine structure should also be taken into account in the calculation of the factor f. In addition, from Fig. 6 it can be seen that, at the higher cesium densities in the D_2 pumping case, the pump-laser frequency was tuned almost completely outside the Doppler core. Because there is some correlation between the emission and reabsorption frequencies (if the emission direction is not at right angles to the absorption direction), the first photon emitted after excitation, in this case, was less likely to be trapped than our simple model predicts. At the very highest densities, the Lorentzian wings also become important in the trapping problem, and taking them into account would further reduce the trapping and therefore increase g. Thus it is not surprising that our model overestimates the ratio $I_{\text{Doppler pedestal}}/I_{\text{narrow spike}}$ in the D_2 case. At low densities, our fitting routine has trouble distinguishing the Doppler pedestal from the wings of the Lorentzian spike. This effect artificially reduces the experimental values of $I_{\text{Doppler pedestal}}/I_{\text{narrow spike}}$ in this limit.

From our model, we can see that at low densities [see Eq. (A3) in the Appendix], both the resonance exchange and radiation trapping terms scale with density. They can only be experimentally distinguished through their dependence on radiation trapping geometry. We are currently constructing new cells in a thin-slab geometry in which we expect that the thermalization due to radiation trapping will be reduced to the point where the resonance exchange collisions can be directly studied. We note that, at higher densities, Eq. (A5) shows that the resonance exchange contribution to the fluorescence ratio grows quadratically, while the radiation trapping term grows linearly with density. However, it is not possible to use this difference to distinguish between the two effects, because in this limit the entire line is thermalized. The selected velocity component (spike) cannot be distinguished from the thermalized background.

CONCLUSIONS

In conclusion, we have presented probe-laser absorption data that show the thermalization of velocity-selected cesium $6\,^2P_{1/2}$ and $6\,^2P_{3/2}$ atoms through the mechanisms of radiation trapping and resonance exchange. The principal purpose of this work is to demonstrate that, in a pure metal vapor, thermalization of velocity-selected excited-atom distributions by these mechanisms can be orders of magnitude greater than that from velocity-changing collisions. We have also presented a model of these phenomena, based on detailed calculations of radiation trapping escape factors, which is in reasonable agreement with the experimental results.

ACKNOWLEDGMENTS

The authors would like to thank Dr. Jinx Cooper, Dr. Andreas Molisch, Dr. Alan Streater, and Dr. A. Peet Hickman for many valuable discussions on this topic. We would like to acknowledge financial support for this work from the National Science Foundation under Grant No. PHY-9119498.

APPENDIX

At low atom densities, where the line-center opacity satisfies $k_0 l<10$ (k_0 is the line-center absorption coefficient and l is the mean escape distance), the escape factor can be calculated using the Milne theory of radiation trapping [23,28],

$$g_j=[1+(\bar{kl}/\varepsilon_j)^2]^{-1}\ . \tag{A1}$$

For the fundamental mode ε_j is the first root of

$$\varepsilon_j\tan(\varepsilon_j)=\bar{kl} \tag{A2}$$

and the mean opacity $\bar{kl}$ is given by Samson's equivalent opacity (see Ref. [29]) modified to include hyperfine structure. Escape factors for higher modes can be obtained from Eq. (A1) using the higher roots of Eq. (A2).

In the limit of very low density, the opacity is small and we can replace $\varepsilon\tan(\varepsilon)$ by ε^2 in Eq. (A2). Then Eq. (A1) for the fundamental mode escape factor reduces to $g\approx1-\bar{kl}$. Thus in this limit the fluorescence ratio is given approximately by

$$\left[\frac{I_{\text{Doppler pedestal}}}{I_{\text{narrow spike}}}\right]_{\text{low density}} = \frac{(k_{\text{VCC}}+k_{\text{RE}})n_{6S}+\bar{kl}f\Gamma_{6P\to6S}}{\Gamma_{6P\to6S}} = \frac{(k_{\text{VCC}}+k_{\text{RE}}+\bar{\sigma l}f\Gamma_{6P\to6S})n_{6S}}{\Gamma_{6P\to6S}}\ , \tag{A3}$$

where we have expressed the mean opacity in terms of an average absorption cross section ($\bar{k}l=\bar{\sigma}ln_{6S}$), and where we have also dropped the factor g from the denominator since it is approximately equal to 1. Thus in the low-density limit, we expect that the ratio of pedestal-to-spike intensity will scale linearly with density.

At higher densities, where $k_0 l > 10$, the Holstein theory of radiation trapping is valid [20,24]. When the trapping is dominated by the Doppler wings of the line, as in the present case, Holstein has shown that, for a cylinder of radius R, the fundamental mode escape factor g is given to lowest order by [24,30]

$$g=\frac{1.575}{k_0R[\pi\ln(k_0R)]^{1/2}} . \tag{A4}$$

Substituting this into Eq. (7) we obtain

$$\left[\frac{I_{\text{Doppler pedestal}}}{I_{\text{narrow spike}}}\right]_{\text{high density}} = \frac{(k_{\text{VCC}}+k_{\text{RE}})n_{6S}+f\Gamma_{6P\to 6S}}{1.575\Gamma_{6P\to 6S}} \times\sigma_0R[\pi\ln(\sigma_0Rn_{6S})]^{1/2}n_{6S} , \tag{A5}$$

where we have set $(1-g)\approx 1$ in this limit, and we have again expressed the (line-center) absorption coefficient in terms of an absorption cross section in order to bring out the density dependence. Since the log term is slowly varying, the fluorescence ratio in this limit can display either a linear or a quadratic dependence on density, depending on whether the radiation trapping or resonance exchange term dominates the right-hand side of Eq. (A5).

[1] P. G. Pappas, M. M. Burns, D. D. Hinshelwood, and M. S. Feld, Phys. Rev. A **21**, 1955 (1980).
[2] C. S. Adams and A. I. Ferguson, Opt. Commun. **75**, 419 (1990).
[3] A. M. Akulshin, A. A. Celikov, and V. L. Velichansky, Opt. Commun. **93**, 54 (1992).
[4] E. Kuchta, R. J. Alvarez II, Y. H. Li, D. A. Krueger, and C. Y. She, Appl. Phys. B **50**, 129 (1990).
[5] K.-D. Heber, P. J. West, and E. Matthias, Phys. Rev. A **37**, 1438 (1988).
[6] S. Chu, L. Hollberg, J. E. Bjorkholm, A. Cable, and A. Ashkin, Phys. Rev. Lett. **55**, 48 (1985).
[7] A. Aspect, E. Arimondo, R. Kaiser, N. Vansteenkiste, and C. Cohen-Tannoudji, Phys. Rev. Lett. **61**, 826 (1988).
[8] C. Monroe, W. Swann, H. Robinson, and C. Wieman, Phys. Rev. Lett. **65**, 1571 (1990).
[9] P. F. Liao, J. E. Bjorkholm, and P. R. Berman, Phys. Rev. A **21**, 1927 (1980).
[10] K. E. Gibble and A. Gallagher, Phys. Rev. A **43**, 1366 (1991).
[11] E. E. Nikitin, in *The Excited State in Chemical Physics,* edited by J. W. McGowan, Advances in Chemical Physics Vol. 28 (Wiley, New York, 1975), pp. 317–377.
[12] C. G. Carrington, D. N. Stacey, and J. Cooper, J. Phys. B **6**, 417 (1973).
[13] G. W. King and J. H. Van Vleck, Phys. Rev. **55**, 1165 (1939).
[14] G. A. Mead, Int. J. Theor. Phys. **1**, 317 (1968).
[15] J. Cooper and D. N. Stacey, Phys. Lett. **46A**, 299 (1973).
[16] K. Ellinger, J. Cooper, and P. Zoller, Phys. Rev. A **49**, 3909 (1994).
[17] A. N. Nesmeyanov, *Vapor Pressure of the Elements* (Academic, New York, 1964).
[18] E. Arimondo, M. Inguscio, and P. Violino, Rev. Mod. Phys. **49**, 31 (1977).
[19] J. Sagle, R. K. Namiotka, and J. Huennekens, J. Phys. B (to be published).
[20] T. Holstein, Phys. Rev. **72**, 1212 (1947).
[21] C. Van Trigt, Phys. Rev. A **13**, 726 (1976).
[22] A. F. Molisch, B. P. Oehry, and G. Magerl, J. Quant. Spectrosc. Radiat. Transfer **48**, 377 (1992).
[23] E. A. Milne, J. London Math. Soc. **1**, 40 (1926).
[24] T. Holstein, Phys. Rev. **83**, 1159 (1951).
[25] A. F. Molisch, B. P. Oehry, W. Schupita, and G. Magerl, J. Quant. Spectrosc. Radiat. Transfer **49**, 361 (1993).
[26] *Handbook of Mathematical Functions,* edited by M. Abramowitz and I. A. Stegun (Dover, New York, 1972).
[27] Z. J. Jabbour, J. Huennekens, M. Allegrini, S. Milosevic, and F. de Tomasi (unpublished).
[28] T. Colbert and J. Huennekens, Phys. Rev. A **41**, 6145 (1990).
[29] A. C. G. Mitchell and M. W. Zemansky, *Resonance Radiation and Excited Atoms* (Cambridge University Press, Cambridge, 1971).
[30] M. G. Payne and J. D. Cook, Phys. Rev. A **2**, 1238 (1970).